Interfacially Stable MOF Nanosheet Membrane with Tailored Nanochannels for Ultrafast and Thermo-Responsive Nanofiltration

Wei Jia[1,2], Baohu Wu[3], Shengtong Sun[1](✉), and Peiyi Wu[1,2](✉)

[1] *State Key Laboratory for Modification of Chemical Fibers and Polymer Materials, College of Chemistry, Chemical Engineering and Biotechnology, Center for Advanced Low-dimension Materials, Donghua University, Shanghai 201620, China*
[2] *State Key Laboratory of Macromolecular Engineering of Polymers, Department of Macromolecular Science, Fudan University, 2205 Songhu Road, Shanghai 200433, China*
[3] *Jülich Centre for Neutron Science (JCNS) at Heinz Maier-Leibnitz Zentrum (MLZ) Forschungszentrum Jülich, Lichtenbergstr. 1, 85748 Garching, Germany*

ABSTRACT

Two-dimensional nanosheet membranes with responsive nanochannels are appealing for controlled mass transfer/separation, but limited by everchanging thicknesses arising from unstable interfaces. Herein, an interfacially stable, thermo-responsive nanosheet membrane is assembled from twin-chain stabilized metal-organic framework (MOF) nanosheets, which function via two cyclic amide-bearing polymers, thermo-responsive poly(N-vinyl caprolactam) (PVCL) for adjusting channel size, and non-responsive polyvinylpyrrolidone for supporting constant interlayer distance. Owing to the microporosity of MOF nanosheets and controllable interface wettability, the hybrid membrane demonstrates both superior separation performance and stable thermo-responsiveness. Scattering and correlation spectroscopic analyses further corroborate the respective roles of the two polymers and reveal the microenvironment changes of nanochannels are motivated by the dehydration of PVCL chains.

KEYWORDS

MOF nanosheet membrane, thermo-responsiveness, molecular separation, IR spectroscopy

1 Introduction

Responsive nanochannels within cell membranes play a crucial role in substance transfer between cells and the extracellular world, which is the fundamental process for the implementation of many biological functions.[1-3] Inspired by cell membranes, significant efforts have been made to develop stimuli-responsive membranes with "smart" nanochannels, which could respond to various stimuli, including temperature, pH, light, CO_2, etc.[4-6] Owing to the merits of dynamic channel size, stimuli-responsive membranes have shown great potential in artificial organs, biological sensors, drug delivery systems, and controlled separation technology.[7, 8] In recent years, in contrast to conventional polymeric materials, two-dimensional (2D) nanosheets are emerging to be more advantageous in developing high-performance stimuli-responsive membranes.[9, 10] Based on the spontaneous orientation of atom-thick 2D nanosheets, a large number of intrinsic nanochannels are formed between stacked nanosheets, which bestow the lamellar membranes with ultrafast water permeation and high selectivity.[11-14] Stimuli-responsiveness can also be easily introduced to 2D nanosheet membranes by introducing stimuli-responsive polymers into the interlayer.[15-18] For example, robust and porous thermo-responsive nanosheet-based hydrogel membranes were prepared by filtrating an aqueous dispersion containing chemically converted graphene and poly(*N*-isopropylacrylamide) (PNIPAM).[15] By adjusting polymer grafting density, PNIPAM-grafted graphene oxide membranes with reversible positive or negative gating regularity have also been constructed.[16, 17] Nevertheless, all the previously reported thermo-responsive nanosheet membranes rely on the *d*-spacing changes caused by the volume transition of single-component thermo-responsive polymers. Despite 'fully smart' interlayer nanochannels, the concomitant thermally vulnerable interfaces significantly decrease membrane stability, leading to everchanging thicknesses and weakened separation performance at high sensitivity level.[19-22] In this regard, interfacial stabilization is highly desired for thermo-responsive nanosheet membranes without sacrificing the membrane's permeance and separation tunability.

Layered metal-organic framework (MOF) nanosheets are a new class of 2D microporous crystalline nanomaterials in the composition of metal ions and organic ligands.[23] Compared to bulk MOF nanoparticles, flexible MOF nanosheets are ideal constructing units for lamellar membranes on account of their nanosized thickness and 2D micromorphology.[24, 25] Importantly, the regularly arranged micropores endow MOF nanosheet membranes with intrinsically superior permeance and high selectivity than other low-porosity nanosheet membranes.[26] Besides, the easy polymer functionalization of MOF nanosheets also brings superior advantages of MOF nanosheet membranes for precisely regulating interlayer properties that may well balance the membrane stability and thermo-responsiveness.[27-29]

Address correspondence to Shengtong Sun, shengtongsun@dhu.edu.cn; Peiyi Wu, wupeiyi@dhu.edu.cn

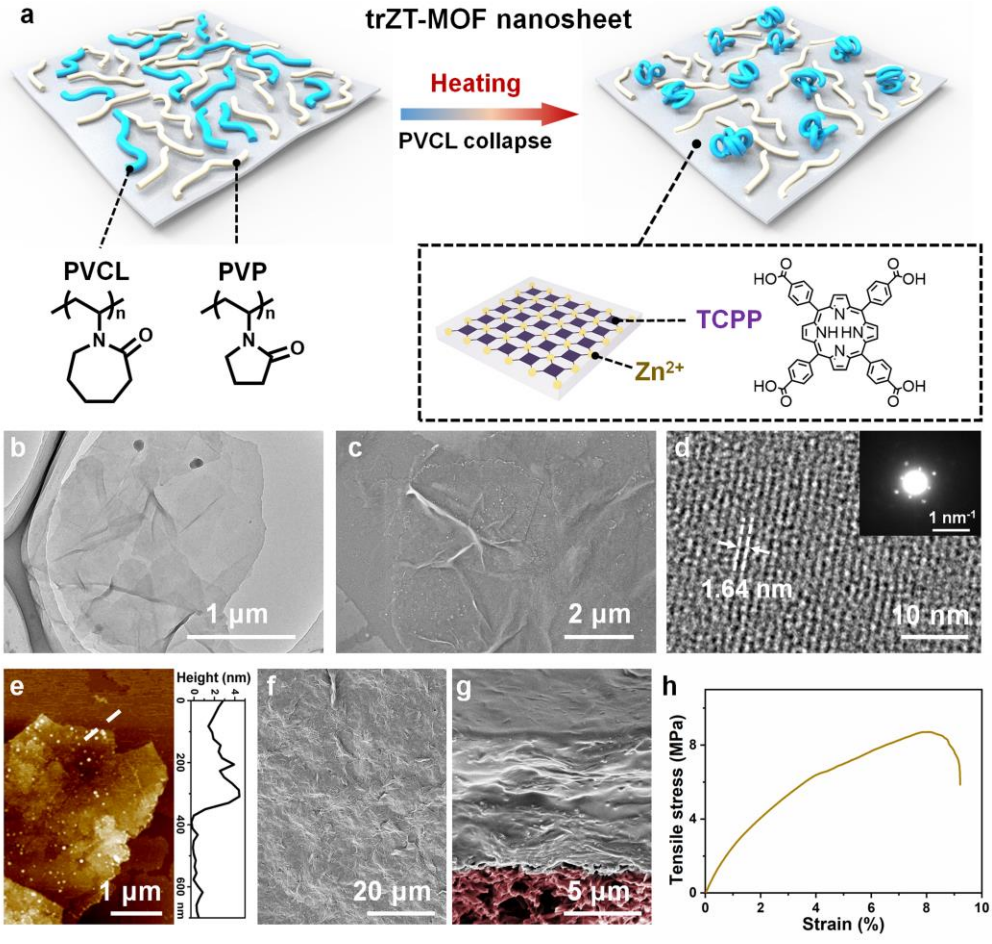

Figure 1. (a) Schematic illustration of the synthesized trZT-MOF nanosheets. (b) HR-TEM and (c) FE-SEM images of trZT-MOF nanosheets. (d) Magnified HR-TEM image of trZT-MOF nanosheet (inset: corresponding SAED pattern). (e) AFM image and height profile of trZT-MOF nanosheets. (f) Surface FE-SEM image of the trZT-MOF nanosheet membrane (~150 nm thick). (g) Cross-sectional FE-SEM image of a thick trZT-MOF nanosheet membrane (~20 μm thick) supported on porous nylon substrate (pink color). (h) Tensile stress-strain curve of free-standing trZT-MOF nanosheet membrane peeled off from (g).

Herein, we report the first example of thermoresponsive yet interfacially stable MOF nanosheet membrane assembled from twin-chain stabilized Zn-tetrakis(4-carboxyphenyl) porphyrin MOF (trZT-MOF; 'tr' means thermoresponsive) nanosheets. The key of our design is to use two stabilizing agents for MOF nanosheets which bear analogous anchoring side cyclic amide groups (Fig. 1a), poly(*N*-vinyl caprolactam) (PVCL), known as a nontoxic lower critical solution temperature (LCST)-type water-soluble polymer, and polyvinylpyrrolidone (PVP), a fully hydrophilic polymer with no response to temperature changes.[30] Such a twin-chain strategy endows the filtrated MOF nanosheet membrane with not only outstanding thermo-responsive separation performance from the reversible collapse of PVCL chains but also high structural stability with constant interlayer distance maintained by PVP chains. Moreover, the abundant micropores in trZT-MOF nanosheets guarantee both superior water permeance and high selectivity at ambient temperatures.

2 Results and discussion

Ultrathin trZT-MOF nanosheets were solvothermally synthesized from $Zn(NO_3)_2$ and tetrakis(4-carboxyphenyl) porphyrin (TCPP) in the presence of PVCL and PVP (1:3 weight ratio) via an attaching and confined growth mechanism.[27, 28] Similar to PVP, PVCL with the same cyclic amide group could simultaneously attach to trZT-MOF surface via strong interactions between C=O groups and Zn^{2+}, and thus confines the z-axial crystal growth of Zn-TCPP MOF. TEM and FE-SEM images clearly show the typical 2D micromorphology of the obtained trZT-MOF nanosheets with an unusual large mean lateral size of 6.5 μm (Fig. 1 b, c, and Fig. S1; schematic crystalline structure in Fig. S2). Wrinkles are also occasionally observed, demonstrating the good flexibility of trZT-MOF nanosheets. The HR-TEM image of the trZT-MOF nanosheet (Fig. 1d) shows the clear lattice fringe with an interplanar distance of 1.64 nm, ascribed to the (100) plane of Zn-TCPP crystal. The good crystallinity of trZT-MOF nanosheets is also evidenced by the selected-area electron diffraction (SAED) pattern and XRD profile (inset in Fig. 1d, and Fig. S3). According to the AFM image, the thickness of the trZT-MOF nanosheet is ca. 3 nm (Fig. 1e), much thinner than previously reported PVP-stabilized Zn-TCPP MOF nanosheets (~7.6 nm)[27]. N_2 adsorption and desorption isotherms (Fig. S4) demonstrate the good intrinsic porosity of trZT-MOF nanosheets with a Brunauer-Emmett-Teller (BET) surface area of 326.6 $m^2 g^{-1}$, higher than bulk Zn-TCPP MOF (197 $m^2 g^{-1}$).[27] Furthermore, the emergence of C=O infrared peaks ascribed to PVCL and PVP indicates the successful inclusion of polymers in trZT-MOF nanosheets (Fig. S5), and TGA estimates the polymer content to be ~35 wt% (Fig. S6). The C=O groups of PVP and PVCL show obvious

peak shifts compared to their bulk state, which could be ascribed to the strong interactions between polymers and MOF nanosheets as well as their confined conformations on the MOF nanosheet surface. The temperature-dependent turbidity measurement suggests that the attached PVCL successfully endows trZT-MOF nanosheets with typical LCST-type thermo-responsibility (LCST ≈ 43 °C, Fig. S7).

The trZT-MOF nanosheet membrane was then fabricated via vacuum-assisted self-assembly technology on nylon substrates. It is noteworthy that the large lateral size of trZT-MOF nanosheets is highly crucial for the production of high-quality defect-free membranes.[31] As shown in Fig. 1f and g, the obtained trZT-MOF nanosheet membrane possesses a very compact surface and a layered structure. Owing to the intertwining polymers between nanosheets serving for strong adhesion, the freestanding trZT-MOF nanosheet membrane is mechanically robust with the tensile strength of 9 MPa and elongation of 9% (Fig. 1h), high enough for practical separation applications.[15]

A 150 nm-thick trZT-MOF nanosheet membrane (cross-sectional SEM image in Fig. S8) was prepared to test its ambient-temperature separation performance under the operating pressure of 1 bar. Here, six solutions with increasing solute sizes, containing NaCl, $CaCl_2$, brilliant green (BG), neutral red (NR), crystal violet (CV), and methyl blue (MB), were used. As shown in Fig. 2a, the separation

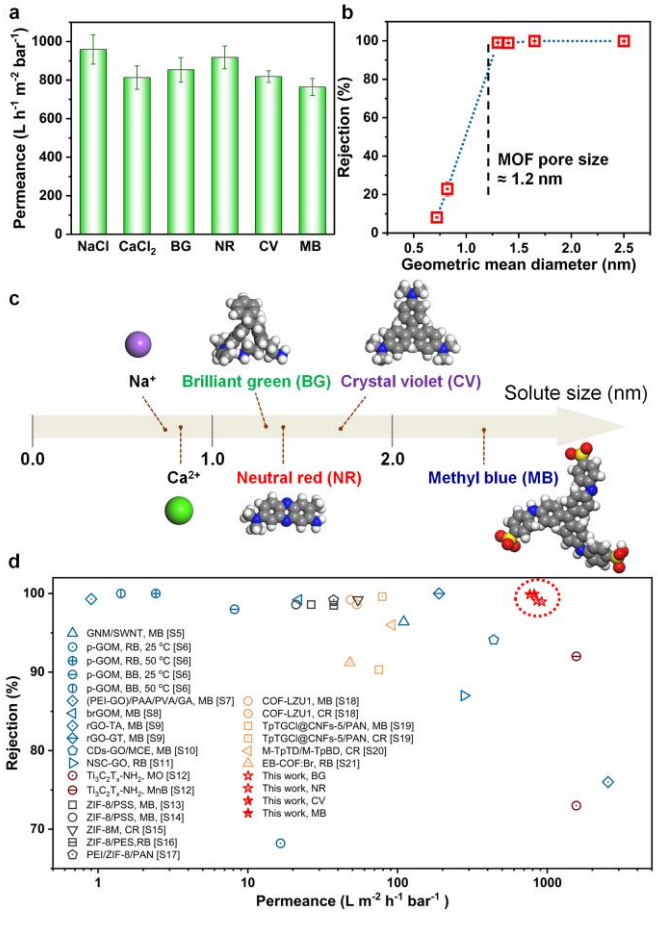

Figure 2. (a) Permeance of trZT-MOF nanosheet membrane as feeding NaCl, $CaCl_2$, neutral red (NR), crystal violet (CV), brilliant green (BG), and methyl blue (MB) solutions. (b) Rejection rates of trZT-MOF nanosheet membrane by feeding with different solutes. (c) Schematic illustration of solutes with different sizes. (d) Membrane separation performance compared with previous reports (see Table S1 for details).

permeance of the trZT-MOF nanosheet membrane at ambient temperature reaches as high as 959 L m^{-2} h^{-1} bar^{-1}. Among the four studied dyes, the highest permeance of NR may be attributed to both its small size and rod-like topology resulting in a low viscous resistance to water. Additionally, a typical size-selective separation is also observed (Fig. 2b and c). According to the crystallographic data, the pore size of Zn-TCPP MOF is around 1.2 nm.[32] Reasonably, when the solute size is larger than the pore size of trZT-MOF nanosheets, there is a sharp increase in the rejection rate of trZT-MOF nanosheet membrane. The rejection rate of Ca^{2+} with a hydrated diameter of 0.82 nm is only 22.9%, while the rejection rate of BG with a diameter of 1.3 nm[33] rapidly rises to 99.0 %. When feeding CV and MB solutions with even larger solute sizes, the rejection rates are more than 99.9%. Such a phenomenon clearly indicates that the intrinsic porous nature of trZT-MOF nanosheets plays an important role in the membrane separation process. Compared with previously reported other 2D nanosheet or MOF-based membranes, trZT-MOF nanosheet membrane simultaneously demonstrates high selectivity and superior separation permeance (see comparison data in Fig. 2d and Table S1). We attribute such good separation performance of trZT-MOF nanosheet membrane to mainly two reasons. First, the existence of a large number of nanochannels from both the orderly stacking nanosheets and the intrinsic microporosity of trZT-MOF nanosheets contributes to the observed high permeance. Second, the highly intertwined polymers attached on MOF nanosheets could effectively eliminate the stacking defects, allowing the size separation capacity of MOF nanopores to truly work.

Benefitting from the LCST phase transition of PVCL chains, the trZT-MOF nanosheet membrane also shows sensitive thermo-responsive separation properties. As shown in Fig. 3a, the pure water permeance of the trZT-MOF nanosheet membrane is positively responsive to temperature changes, which largely increases from 858 L m^{-2} h^{-1} bar^{-1} at 20 °C to 1934 L m^{-2} h^{-1} bar^{-1} at 70 °C. Upon several cycles between 30 and 60 °C, the trZT-MOF nanosheet membrane still demonstrates good thermo-responsive reversibility (Fig. 3b). Upon being immersed in water at different temperatures, no obvious peak shifts could be observed in the XRD profiles, which demonstrates the good stability of the trZT-MOF nanosheet membrane in water (Fig. S9). To test the ability of the trZT-MOF nanosheet membrane for thermo-responsive separation of different substances, three dye solutions with very close solute sizes, BG, NR, and CV, were fed separately at varying temperatures. As temperature rises from 20 to 70 °C, the permeance of the trZT-MOF nanosheet membrane increases while the rejection rates decrease when feeding all the three dye solutions (Fig. 3c and d). For example, the permeance of NR solution increases from 885 to 1532 L m^{-2} h^{-1} bar^{-1}, while its rejection rate decreases from 99.0% to 1.3%. The reduction of the rejection rates of smaller dyes like BG (1.3 nm) and NR (1.4 nm) is much faster than CV with a slightly larger size (1.6 nm), suggesting that the size dependence of membrane separation performance is retained even upon drastic interlayer disturbance. The lowest rejection rate of NR after heating might be caused by its rod-like topology (Fig. 2c). The decreased rejection rates of dyes

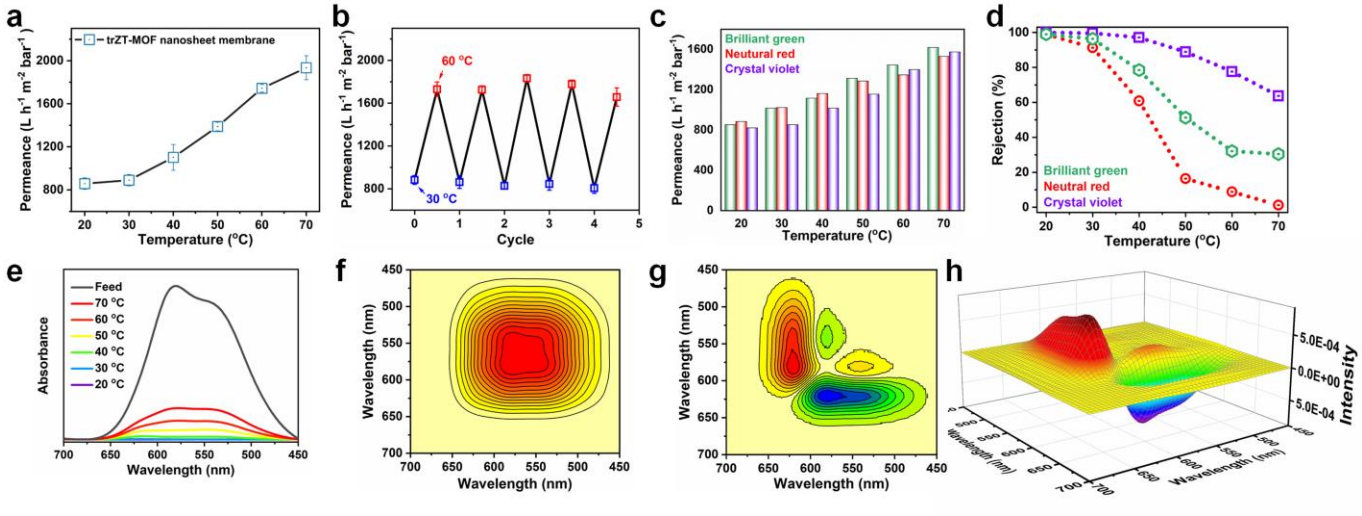

Figure 3. (a) Temperature-dependent water permeance of trZT-MOF nanosheet membrane from 20 to 70 °C. (b) Thermo-responsive stability test of trZT-MOF nanosheet membrane. (c) Temperature-dependent permeance and (d) rejection rates of trZT-MOF nanosheet membrane when feeding different dye solutions. (e) UV/vis spectra of the feed mixed dye solution (NR/CV/BG, 10/10/10 ppm) and filtrates at different temperatures. (f) Synchronous and (g) asynchronous 2D correlation UV/vis spectra generated from the 1D spectra of filtrates in (e). (h) is the 3D plot of the asynchronous spectrum.

larger than 1.2 nm upon heating further demonstrates that the polymers (PVP and PVCL) exist on the MOF nanosheet surface rather than in the pores; that is, the collapse of PVCL chains increases the size of separation nanochannels, enabling dyes with larger sizes than MOF pores to permeate, too. Besides, the trZT-MOF nanosheet membrane shows also good thermo-responsive reversibility of dye rejection (Fig. S10).

A mixed dye solution (BG/NR/CV, 10/10/10 ppm) was fed at varying temperatures to evaluate the thermo-responsive separation performance of the trZT-MOF nanosheet membrane for distinguishing substances in mixtures. 2D correlation UV/vis spectra, generated from the temperature-dependent 1D UV/vis spectra of filtrates (Fig. 3e), were used to determine the outflow sequence of three dyes upon heating. As shown in Fig. 3f-h, three absorption peaks at 541, 579, and 622 nm are observed in the 2D correlation UV/vis spectra, which are ascribed to NR, CV, and BG (see their individual spectra in Fig. S11), respectively. Judging from Noda's rule[34, 35], the thermo-responsive sequence is, 622 → 541 → 579 nm (→ represents prior to). In other words, BG and NR pass through the membrane first, followed by CV in the mixture. Since the absolute zeta-potential value of the trZT-MOF membrane is relatively low (Fig. S12), the separation performance of the trZT-MOF membrane mainly depends on size sieving. The transfer sequence of the three dye molecules upon heating further proves that the nanochannel size of the trZT-MOF nanosheet membrane continuously increases with temperature, highlighting its thermo-responsibility for separation applications. Pure substances with even close molecular sizes may be obtained by repeated filtration regulated by temperature as an additional controlling factor.

To further understand the thermo-responsive nature of the trZT-MOF nanosheet membrane, temperature-dependent small-angle X-ray scattering (SAXS), and FTIR spectroscopy were carried out. As shown in Fig. 4a and Fig. S13, there appears a remarkable SAXS peak in the high q range (scattering vector q = 3.73 nm^{-1}), which is related to the *d*-distance of 1.68 nm ($d = 2\pi/q$) for trZT-MOF nanosheet membrane along the (001) direction. During heating, the position of this peak is almost unchanged, suggesting the membrane's constant interlayer distance and excellent structural stability. This is also supported by the unnoticeable membrane thickness changes in many heating-cooling cycles (data not shown). The collapse of PVCL chains seems only to increase the nanochannel size as PVP chains fully stabilize the interlayer distance. Moreover, we also observed the whole rising of the absolute scattering intensities at q > 1 nm^{-1} (Fig. S13). The gradual increase of the calculated Porod constant[36] with temperature clearly demonstrates the increasing specific area of trZT-MOF nanosheets, caused by the partial collapse of the polymer network (Fig. S14). Therefore, it is presumed to be the volume shrinkage of PVCL that allows more pores on trZT-MOF nanosheets to be exposed so that additional separation nanochannels are formed in the membrane.

FTIR spectroscopy is very sensitive to molecular-level changes and powerful to explore the thermo-responsive group motions. From temperature-dependent FTIR spectra of C=O region (Fig. 4b), five different peaks could be distinguished at 1666 cm^{-1} (dehydrated, PVCL), 1643 cm^{-1} (hydrogen bonded, PVCL), 1622 cm^{-1} (PVP), 1599 cm^{-1} (dehydrated, MOF), and 1583 cm^{-1} (hydrogen bonded, MOF).[28, 37, 38] As shown in Fig. 4b, c and Fig. S15, the C=O peaks ascribed to both PVCL and MOF show binary intensity changes (corresponding to the transformation of hydrogen bonded groups to dehydrated ones) with 'S-shaped' variation trends, typical for LCST-type phase transitions.[39, 40] The simultaneous changes of MOF and PVCL reveal the significant influence of PVCL chain collapse on the interfacial properties of MOF nanosheets. That is, the surrounding environment of MOF nanosheets becomes less hydrated due to the

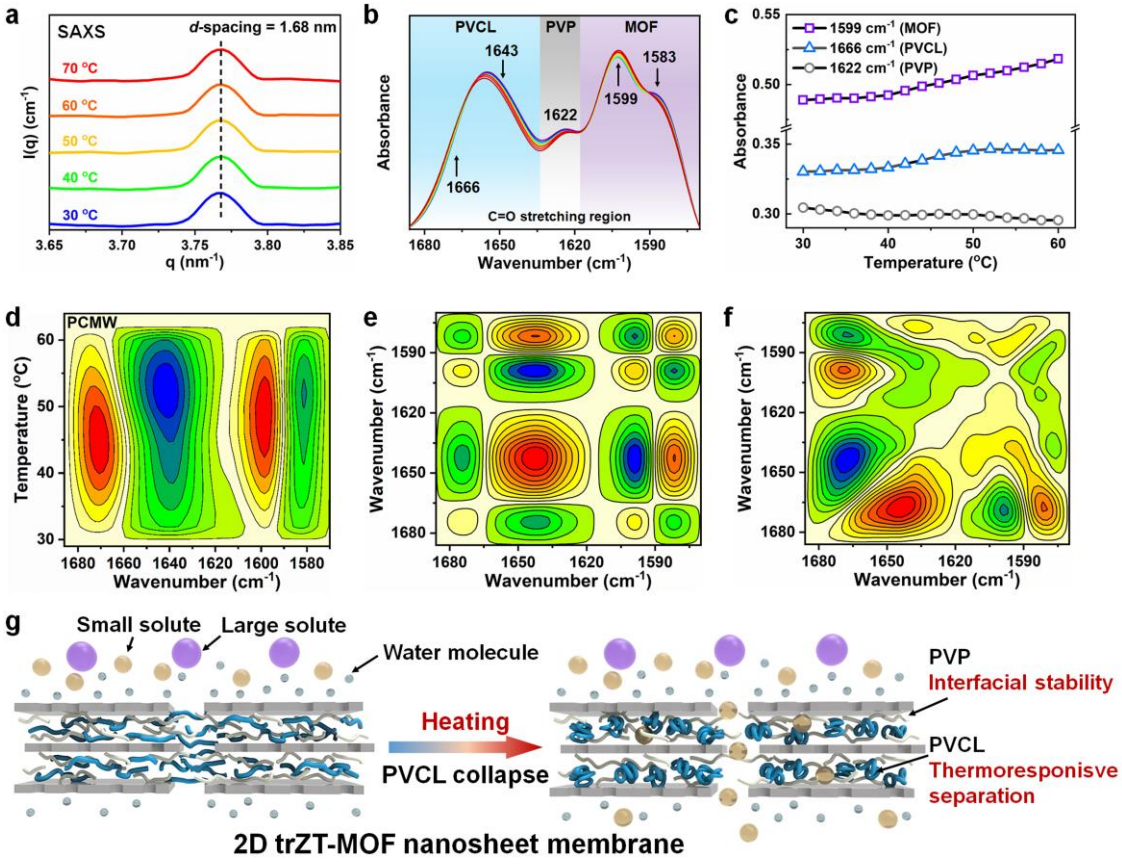

Figure 4. (a) Temperature-dependent SAXS profiles of the trZT-MOF nanosheet membrane indicate a constant interlayer *d*-spacing of 1.68 nm. (b) Temperature-dependent FTIR spectra of the trZT-MOF membrane (30-60 °C). The arrows indicate the spectral variation trends at different wavenumbers. (c) Temperature-dependent spectral intensity changes of ν(C=O) from MOF, PVCL, and PVP. (d) PCMW synchronous spectrum of the trZT-MOF nanosheet membrane. (e) Synchronous and (f) asynchronous 2D correlation FTIR spectra of trZT-MOF nanosheet membrane generated from the 1D spectra in (b). (g) Schematic illustration of the "smart" membrane separation performance of the trZT-MOF nanosheet membrane with thermo-responsive nanochannels. PVP and PVCL serve for interfacial stability and thermoresponsive separation, respectively.

significant dehydration of PVCL chains, reflected by the IR spectral intensity changes of C=O groups. In contrast, the C=O peak intensity of PVP shows only a slight decrease during heating, suggesting that PVP does not actively participate in the LCST transition, consistent with its interlayer-supporting role.

The perturbation correlation moving window (PCMW) technique was utilized to visualize the subtle changes of the whole spectral region at a high resolution.[41] From PCMW synchronous spectrum (Fig. 4d), the phase transition temperatures of PVCL and MOF can be read out to be 44-52 °C, slightly higher than that of trZT-MOF nanosheets (≈ 43 °C) perhaps due to more structural constraints in the membrane. On the other hand, no PVP-related temperatures can be observed, indicating that PVP chains do not change in this process, in accordance with 1D spectral analysis. 2D correlation FTIR spectroscopy was also employed to determine the responsive sequence of various functional groups.[34, 35] According to the signs of cross-peaks in 2D correlation synchronous and asynchronous spectra (Fig. 4e and f, see details in supporting information), the sequence is determined to be, 1666 → 1583 → 1643 → 1599 cm^{-1} (→ represents prior to), or ν(dehydrated C=O, PVCL) → ν(hydrogen bonded C=O, MOF) → ν(hydrogen bonded C=O, PVCL) → ν(dehydrated C=O, MOF). Obviously, the thermo-responsibility of the trZT-MOF nanosheet membrane is motivated by the dehydration or aggregation of PVCL chains, which further decreases the interfacial wettability of MOF nanosheets accompanied by exposing more nanochannels. Schematic illustration of the inferred mechanism is thus presented in Fig. 4g to show the respective roles of PVCL and PVP chains for the thermo-responsive separation of the trZT-MOF nanosheet membrane. Except for the exposed more nanochannels upon heating, low viscous resistance to water molecules due to the dehydrated PVCL and MOF may also contribute to the significant permeance increase at high temperatures.[42]

3 Conclusions

In summary, an interfacially stable 2D MOF nanosheet membrane with thermoresponsive nanochannels is successfully developed via a twin-chain stabilizing strategy. Two kinds of polymers, PVCL, and PVP, containing analogous cyclic amide groups, are first used to assist the synthesis of thermo-responsive, large-size MOF nanosheets. Besides good mechanical toughness and outstanding ambient-temperature separation performance, the filtrated trZT-MOF nanosheet membrane exhibits thermo-responsive membrane separation properties with unexpected structural stability, which was never realized before. The respective roles of PVCL and PVP for thermo-responsibility and interfacial stability were also elucidated from scattering and spectroscopic studies, highlighting the validity of our design. It is anticipated that the present interface engineering method may inspire the development of next-generation, high-performance nanosheet-based hybrid membranes with stably

integrated interfaces and responsive nanochannels for accurately controlled separation applications.

Acknowledgements

The authors gratefully acknowledge the financial support from the National Science Foundation of China (Nos. 21991123, 51733003, 21674025, 51873035), and "Qimingxing" project (No. 19QA1400200) of the Shanghai Committee of Science and Technology. The authors also thank the staff from BL16B Beamline at the Shanghai Synchrotron Radiation Facility for assistance during data collection.

Electronic Supplementary Material: Supplementary material (Materials and methods, morphology, structure, composition, and thermo-responsiveness characterizations of trZT-MOF nanosheets and membranes. Performance comparison of the trZT-MOF nanosheet membrane with previously reported works) is available in the online version of this article at http://dx.doi.org/10.1007/s12274-***-****-* (automatically inserted by the publisher).

References

[1] Song, W.; Joshi, H.; Chowdhury, R.; Najem, J. S.; Shen, Y.; Lang, C.; Henderson, C. B.; Tu, Y.; Farell, M.; Pitz, M. E.et al. Artificial water channels enable fast and selective water permeation through water-wire networks. *Nat. Nanotechnol*. **2020**, *15*, 73.

[2] Huang, K.; Szleifer, I. Design of multifunctional nanogate in response to multiple external stimuli using amphiphilic diblock copolymer. *J. Am. Chem. Soc*. **2017**, *139*, 6422-6430.

[3] Hou, X.; Guo, W.; Jiang, L. Biomimetic smart nanopores and nanochannels. *Chem. Soc. Rev*. **2011**, *40*, 2385-2401.

[4] Menne, D.; Pitsch, F.; Wong, J. E.; Pich, A.; Wessling, M. Temperature-modulated water filtration using microgel-functionalized hollow-fiber membranes. *Angew. Chem., Int. Ed*. **2014**, *53*, 5706-5710.

[5] Zhu, Z.; Wang, D.; Tian, Y.; Jiang, L. Ion/molecule transportation in nanopores and nanochannels: from critical principles to diverse functions. *J. Am. Chem. Soc*. **2019**, *141*, 8658-8669.

[6] Che, H.; Huo, M.; Peng, L.; Fang, T.; Liu, N.; Feng, L.; Wei, Y.; Yuan, J. CO_2-responsive nanofibrous membranes with switchable oil/water wettability. *Angew. Chem., Int. Ed*. **2015**, *54*, 8934-8938.

[7] Zhou, K. G.; Vasu, K. S.; Cherian, C. T.; Neek-Amal, M.; Zhang, J. C.; Ghorbanfekr-Kalashami, H.; Huang, K.; Marshall, O. P.; Kravets, V. G.; Abraham, J.et al. Electrically controlled water permeation through graphene oxide membranes. *Nature* **2018**, *559*, 236.

[8] Gao, J.; Feng, Y.; Guo, W.; Jiang, L. Nanofluidics in two-dimensional layered materials: inspirations from nature. *Chem. Soc. Rev*. **2017**, *46*, 5400-5424.

[9] Yang, Y.; Yang, X.; Liang, L.; Gao, Y.; Cheng, H.; Li, X.; Zou, M.; Cao, A.; Ma, R.; Yuan, Q.et al. Large-area graphene-nanomesh/carbon-nanotube hybrid membranes for ionic and molecular nanofiltration. *Science* **2019**, *364*, 1057.

[10] Cai, J.; Li, C.; Kong, N.; Lu, Y.; Lin, G.; Wang, X.; Yao, Y.; Manners, I.; Qiu, H. Tailored multifunctional micellar brushes via crystallization-driven growth from a surface. *Science* **2019**, *366*, 1095.

[11] Kang, Y.; Xia, Y.; Wang, H.; Zhang, X. 2D laminar membranes for selective water and ion transport. *Adv. Funct. Mater*. **2019**, *29*, 1902014.

[12] Wu, X.; Cui, X.; Wu, W.; Wang, J.; Li, Y.; Jiang, Z. Elucidating ultrafast molecular permeation through well-defined 2D nanochannels of lamellar membranes. *Angew. Chem., Int. Ed*. **2019**, *58*, 18524-18529.

[13] Li, Z.; Wei, Y.; Gao, X.; Ding, L.; Lu, Z.; Deng, J.; Yang, X.; Caro, J.; Wang, H. Antibiotics separation with MXene membranes based on regularly stacked high-aspect-ratio nanosheets. *Angew. Chem., Int. Ed*. **2020**, *59*, 2-8.

[14] Wang, S.; Yang, L.; He, G.; Shi, B.; Li, Y.; Wu, H.; Zhang, R.; Nunes, S.; Jiang, Z. Two-dimensional nanochannel membranes for molecular and ionic separations. *Chem. Soc. Rev*. **2020**, *49*, 1071-1089.

[15] Wang, Y.; Chen, S.; Qiu, L.; Wang, K.; Wang, H.; Simon, G. P.; Li, D. Graphene-directed supramolecular assembly of multifunctional polymer hydrogel membranes. *Adv. Funct. Mater*. **2015**, *25*, 126-133.

[16] Liu, J.; Wang, N.; Yu, L.; Karton, A.; Li, W.; Zhang, W.; Guo, F.; Hou, L.; Cheng, Q.; Jiang, L.et al. Bioinspired graphene membrane with temperature tunable channels for water gating and molecular separation. *Nat. Commun*. **2017**, *8*, 2011.

[17] Liu, J.; Yu, L.; Yue, G.; Wang, N.; Cui, Z.; Hou, L.; Li, J.; Li, Q.; Karton, A.; Cheng, Q.et al. Thermoresponsive graphene membranes with reversible gating regularity for smart fluid control. *Adv. Funct. Mater*. **2019**, *29*, 1808501.

[18] Liu, H.; Zhu, J.; Hao, L.; Jiang, Y.; van der Bruggen, B.; Sotto, A.; Gao, C.; Shen, J. Thermo- and pH-responsive graphene oxide membranes with tunable nanochannels for water gating and permeability of small molecules. *J. Membr. Sci*. **2019**, *587*, 117163.

[19] Abraham, J.; Vasu, K. S.; Williams, C. D.; Gopinadhan, K.; Su, Y.; Cherian, C. T.; Dix, J.; Prestat, E.; Haigh, S. J.; Grigorieva, I. V.et al. Tunable sieving of ions using graphene oxide membranes. *Nat. Nanotechnol*. **2017**, *12*, 546.

[20] Hirunpinyopas, W.; Prestat, E.; Worrall, S. D.; Haigh, S. J.; Dryfe, R. A. W.; Bissett, M. A. Desalination and nanofiltration through functionalized laminar MoS_2 membranes. *ACS Nano* **2017**, *11*, 11082-11090.

[21] Ding, L.; Li, L.; Liu, Y.; Wu, Y.; Lu, Z.; Deng, J.; Wei, Y.; Caro, J.; Wang, H. Effective ion sieving with $Ti_3C_2T_x$ MXene membranes for production of drinking water from seawater. *Nat. Sustain*. **2020**, *3*, 296–302.

[22] Ries, L.; Petit, E.; Michel, T.; Diogo, C. C.; Gervais, C.; Salameh, C.; Bechelany, M.; Balme, S.; Miele, P.; Onofrio, N.et al. Enhanced sieving from exfoliated MoS_2 membranes via covalent functionalization. *Nat. Mater*. **2019**, *18*, 1112.

[23] Jr. Denny, M. S.; Moreton, J. C.; Benz, L.; Cohen, S. M. Metal-organic frameworks for membrane-based separations. *Nat. Rev. Mater*. **2016**, *1*, 16078.

[24] Peng, Y.; Li, Y.; Ban, Y.; Yang, W. Two-dimensional metal-organic framework nanosheets for membrane-based gas separation. *Angew. Chem., Int. Ed*. **2017**, *56*, 9757-9761.

[25] Wu, S.; Xin, Z.; Zhao, S.; Sun, S. High-throughput droplet microfluidic synthesis of hierarchical metal-organic framework nanosheet microcapsules. *Nano Res*. **2019**, *12*, 2736-2742.

[26] Peng, Y.; Li, Y.; Ban, Y.; Jin, H.; Jiao, W.; Liu, X.; Yang, W. Metal-organic framework nanosheets as building blocks for molecular sieving membranes. *Science* **2014**, *346*, 1356-1359.

[27] Zhao, M.; Wang, Y.; Ma, Q.; Huang, Y.; Zhang, X.; Ping, J.; Zhang, Z.; Lu, Q.; Yu, Y.; Xu, H.et al. Ultrathin 2D metal-organic framework nanosheets. *Adv. Mater*. **2015**, *27*, 7372-7378.

[28] Wang, Y.; Zhao, M.; Ping, J.; Chen, B.; Cao, X.; Huang, Y.; Tan, C.; Ma, Q.; Wu, S.; Yu, Y.et al. Bioinspired design of ultrathin 2D bimetallic metal-organic-framework nanosheets used as biomimetic enzymes. *Adv. Mater*. **2016**, *28*, 4149-4155.

[29] Zhao, M.; Huang, Y.; Peng, Y.; Huang, Z.; Ma, Q.; Zhang, H. Two-dimensional metal-organic framework nanosheets: synthesis and applications. *Chem. Soc. Rev*. **2018**, *47*, 6267-6295.

[30] Sun, S.; Wu, P. Infrared spectroscopic insight into hydration behavior of poly(n-vinylcaprolactam) in water. *J. Phys. Chem. B* **2011**, *115*, 11609-11618.

[31] Peng, Y.; Li, Y.; Ban, Y.; Jin, H.; Jiao, W.; Liu, X.; Yang, W. Metal-organic framework nanosheets as building blocks for molecular sieving membranes. *Science* **2014**, *346*, 1356-1359.

[32] Choi, E.; Wray, C. A.; Hu, C.; Choe, W. Highly tunable metal-organic frameworks with open metal centers. *Crystengcomm* **2009**, *11*, 553-555.

[33] Tansel, B. Significance of thermodynamic and physical characteristics on permeation of ions during membrane separation: hydrated radius, hydration free energy and viscous effects. *Sep. Purif. Technol*. **2012**, *86*, 119-126.

[34] Noda, I.; Ozaki, Y. *Two-dimensional correlation spectroscopy: applications in vibrational and optical spectroscopy*; John Wiley & Sons, Chichester, **2004**.

[35] Sun, S.; Wu, P. Spectral insights into microdynamics of thermoresponsive polymers from the perspective of two-dimensional correlation spectroscopy. *Chinese J. Polym. Sci*. **2017**, *35*, 700-712.

[36] Blundell, D. J.; Eeckhaut, G.; Fuller, W.; Mahendrasingam, A.; Martin, C. Real time SAXS/stress-strain studies of thermoplastic polyurethanes at large strains. *Polymer* **2002**, *43*, 5197-5207.

[37] Hou, L.; Wu, P. LCST transition of PNIPAM-b-PVCL in water: cooperative aggregation of two distinct thermally responsive segments. *Soft Matter* **2014**, *10*, 3578-3586.

[38] Sethia, S.; Squillante, E. Solid dispersion of carbamazepine in PVPK30 by conventional solvent evaporation and supercritical methods. *Int. J. Pharm.* **2004**, *272*, 1-10.

[39] Sun, S.; Wu, P. Role of water/methanol clustering dynamics on thermosensitivity of poly(n-isopropylacrylamide) from spectral and calorimetric insights. *Macromolecules* **2010**, *43*, 9501-9510.

[40] Sun, S.; Wu, P. On the thermally reversible dynamic hydration behavior of oligo(ethylene glycol) methacrylate-based polymers in water. *Macromolecules* **2013**, *46*, 236-246.

[41] Morita, S.; Shinzawa, H.; Noda, I.; Ozaki, Y. Perturbation-correlation moving-window two-dimensional correlation spectroscopy. *Appl. Spectrosc*. **2006**, *60*, 398-406.

[42] Ladet, S.; David, L.; Domard, A. Multi-membrane hydrogels. *Nature* **2008**, *452*, 76.

.

Electronic Supplementary Material

Interfacially Stable MOF Nanosheet Membrane with Tailored Nanochannels for Ultrafast and Thermo-Responsive Nanofiltration

Wei Jia[1,2], Baohu Wu[3], Shengtong Sun[1](✉), and Peiyi Wu[1, 2](✉)

[1] *State Key Laboratory for Modification of Chemical Fibers and Polymer Materials, College of Chemistry, Chemical Engineering and Biotechnology, Center for Advanced Low-dimension Materials, Donghua University, Shanghai 201620, China*
[2] *State Key Laboratory of Macromolecular Engineering of Polymers, Department of Macromolecular Science, Fudan University, 2205 Songhu Road, Shanghai 200433, China*
[3] *Jülich Centre for Neutron Science (JCNS) at Heinz Maier-Leibnitz Zentrum (MLZ) Forschungszentrum Jülich, Lichtenbergstr. 1, 85748 Garching, Germany*

Supporting information to DOI 10.1007/s12274-****-****-* (automatically inserted by the publisher)

Experimental Section

Materials. Tetrakis(4-carboxyphenyl)porphyrin) (TCPP) and polyvinylpyrrolidone (PVP, M_w ~ 40,000 g/mol) were bought from Tokyo Chemical Industry. Zinc nitrate hexahydrate ($Zn(NO_3)_2{\cdot}6H_2O$), pyrazine, Mowiol® PVA-224 (M_w ~ 205,000 g/mol), *N*-vinylcaprolactam (VCL), 2,2'-azobis(2-methylpropionamidine) dihydrochloride (AIBA), neutral red (NR), crystal violet (CV), methyl blue (MB), and brilliant green (BG) were purchased from Aladdin. Dimethylformamide (DMF) and ethanol were obtained from Sinopharm Chemical Reagent. Nylon filtration membranes (MFNY047022, diameter ~ 47 mm, pore ~ 220 nm) were bought from Tansoole.

Polymerization of VCL. PVCL was synthesized via the radical polymerization of VCL. First, 4 g of VCL was dissolved in 300 mL of water, and N_2 was inflated into the obtained solution for 1 h to remove oxygen. Then, the solution was heated to 70 °C, and 5 mL of AIBA solution (16 mg/mL) was added to the VCL solution. Finally, polymerization was conducted at 70 °C for 8 h. The obtained PVCL was purified via dialysis.

Synthesis of trZT-MOF nanosheets. The synthetic method was modified based on the previous report.[S1] Briefly, $Zn(NO_3)_2{\cdot}6H_2O$ (337.5 mg), pyrazine (60 mg), PVP (1.125 g), and PVCL (375 mg) were dissolved in 300 mL of mixed solvent (225 mL DMF + 75 mL ethanol) to obtain solution A. Then, 300 mg of TCPP was dissolved in 100 mL of mixed solvent (225 mL DMF + 75 mL ethanol) to obtain solution B. Solution B was added to solution A, followed by sonication for 30 min. After that, the obtained mixture was transferred into a PTFE capped reactor, which was kept at 80 °C for 16 h. The synthesized trZT-MOF nanosheets were collected by centrifugation and washed with methanol three times. Finally, trZT-MOF nanosheets were dispersed in methanol. Bulk Zn-TCPP MOF was similarly synthesized without adding PVP and PVCL.

Fabrication of trZT-MOF nanosheet membrane. For 100 nm thick membrane, 0.75 mL of 1.1 mg/mL trZT-MOF nanosheet dispersion in methanol and 1.5 mL of 12 mg/mL PVA solution were added into 50 mL of water. The mixture was sonicated for 10 min. Then, trZT-MOF nanosheet membrane was fabricated on a nylon filtration membrane (diameter, 47 mm; pore size, 220 nm) by filtrating the obtained mixture at 0.2 bar, and then washed with abundant water via filtration at 1 bar. Here, PVA was introduced to assist with the formation of nanosheet membrane, but largely removed during filtration. The membranes with other thicknesses were prepared by controlling the concentration of trZT-MOF nanosheet dispersion.

Characterizations. High-resolution transmission electron microscopy (HR-TEM) images and energy-dispersive X-ray spectrometry (EDX) data were collected on a JEOL JEM2011 at 200 kV. Normal TEM images were taken on FEI Tecnai G2 20 TWIN. Zeiss Ultra 55 was used to capture the field-emission scanning electron microscope (FE-SEM) images. Atomic force microscopy (AFM) images were acquired on Bruker Multimode 8 in tapping mode. X-ray diffraction (XRD) profile was recorded on Bruker D8 ADVANCE. Temperature-dependent Fourier transform infrared (FTIR) spectra were collected on Thermofisher NEXUS 6700 in transmission mode with a resolution of 4 cm^{-1}, 32 scans, and temperature increment of 2 °C. Thin trZT-MOF nanosheet membrane swollen by deuterated water (D_2O) was sealed between two ZnS tablets for the test. Thermogravimetric analysis (TGA) was performed on Mettler Toledo TGA 1 at N_2 atmosphere with a heating rate of 20 °C/min. The temperature-dependent turbidity measurement was taken on a Lambda 35 UV-vis spectrometer at 500 nm, and temperature was controlled by a water-jacketed cell holder. The N_2 adsorption and desorption isotherms of MOF nanosheets were measured by Micrometer ASAP 2420 Adsorption Apparatus. SAXS experiments were conducted at the SSRF beamline BL16B at an X-ray energy of 10.0 keV corresponding to a wavelength of λ = 1.24 Å, where temperature was controlled with a customized temperature-controlling hot stage. For measurement, the swollen membrane was placed in water and sealed in a sandwich cell with two PI windows, where the cell thickness is around 1 mm.
The Porod constant (P)[S2] was determined by Equation (1):

$$\lim_{q\to\infty}(q) * q^4 = P = 2\pi(\Delta\rho)^2 \ S/V \quad (1)$$

Address correspondence to Shengtong Sun, shengtongsun@dhu.edu.cn; Peiyi Wu, wupeiyi@dhu.edu.cn

where S, V and $(\Delta\rho)^2$ represent the surface, volume, and scattering contrast of samples, respectively.

Membrane separation tests. The separation performance of trZT-MOF nanosheet membrane was tested on a home-made dead-end filtration device with an effective area of 9.6 cm^2 under 1 bar operating pressure. All the membranes were pre-compacted by deionized water under 1 bar for 0.5 h to reach a stable water permeance before the test. For each ambient-temperature separation test, 100 mL of feed solution was used, and three independently prepared membranes were tested. One membrane was measured three times for the thermo-responsive reversibility test. The concentration of salt (NaCl and $CaCl_2$) solutions was 100 mg L^{-1}. The concentration of organic dye (NR, MB, CV, and BG) solutions was 10 ppm. The permeance (P, L m^{-2} h^{-1} bar^{-1}) was determined by Equation (2):

$$P = \frac{V}{S*t*p} \quad (2)$$

where V, S, t, and p represent the permeate volume, effective membrane area, filtration time, and operating pressure, respectively.
10 mL of permeate was collected for analyzing the concentration. The concentration of feed (C_f) and permeate (C_p) was determined on Perkin-Elmer Lambda 750. The rejection rate (R) was calculated from Equation (3):

$$R = \left(1 - \frac{C_p}{C_f}\right) * 100\% \quad (3)$$

Perturbation correlation moving window (PCMW). FT-IR spectra collected with an increment of 2 °C during heating process (30-60 °C) were used to perform PCMW analysis. Primary data processing was carried out based on the method provided by Morita, and further correlation calculation was performed using the software 2D Shige, version 1.3 (Shigeaki Morita, Kwansei-Gakuin University, Japan, 2004-2005). The final contour maps were plotted by Origin program, version 2018, with warm colors (red and yellow) defined as positive intensities and cool colors (green and blue) defined as negative ones.
By means of PCMW method, the conventional FTIR spectra can offer a pair of synchronous and asynchronous correlations between spectral and temperature variables. The positive synchronous correlation represents the increased spectral intensity, while the negative synchronous correlation demonstrates a decrease in spectral intensity.[S3] The temperature with the strongest spectral intensity at the specific wavenumber in PCMW synchronous spectrum can be used to determine the transition temperature of corresponding chemical groups.

2D correlation spectroscopy. Temperature-dependent UV/vis and FT-IR spectra were used to perform 2D correlation analysis. 2D correlation analysis was carried out using the same software 2D Shige, version 1.3 (Shigeaki Morita, Kwansei-Gakuin University, Japan, 2004–2005), and was further plotted into the contour maps by the Origin program, version 2018. In the contour maps, warm colors (red and yellow) are defined as positive intensities, while cool colors (green and blue) are defined as negative ones.
2D correlation spectra include two types of correlation maps, synchronous and asynchronous spectra.[S4] Synchronous spectrum shows simultaneous changes between two wavelengths in UV/vis spectra (wavenumbers in FTIR spectra), while asynchronous spectrum can significantly enhance the spectral resolution. The judging rule of the responding sequence is based on Noda's rule- that is, if the multiplication of the signs of cross-peaks (ν_1, ν_2, and assume $\nu_1 > \nu_2$) in synchronous and asynchronous spectra is positive, the change at ν_1 occurs prior to ν_2, and vice versa.

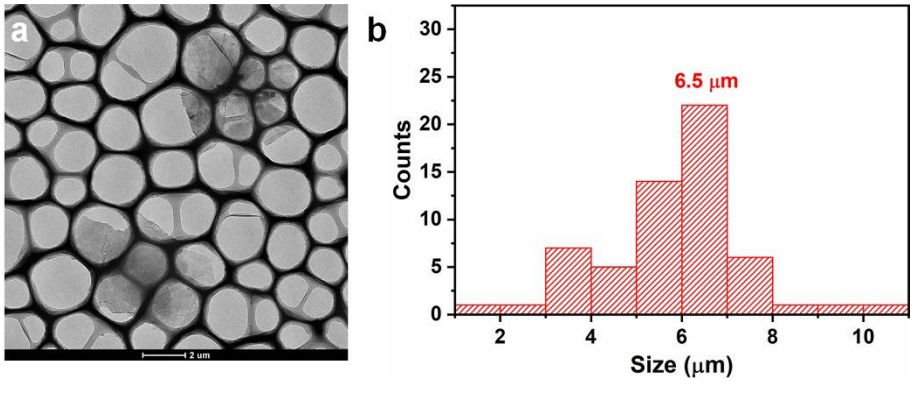

Figure S1. a) TEM images of trZT-MOF nanosheets. b) Statistical analysis of the lateral sizes of trZT-MOF nanosheets shows a mean size of 6.5 μm.

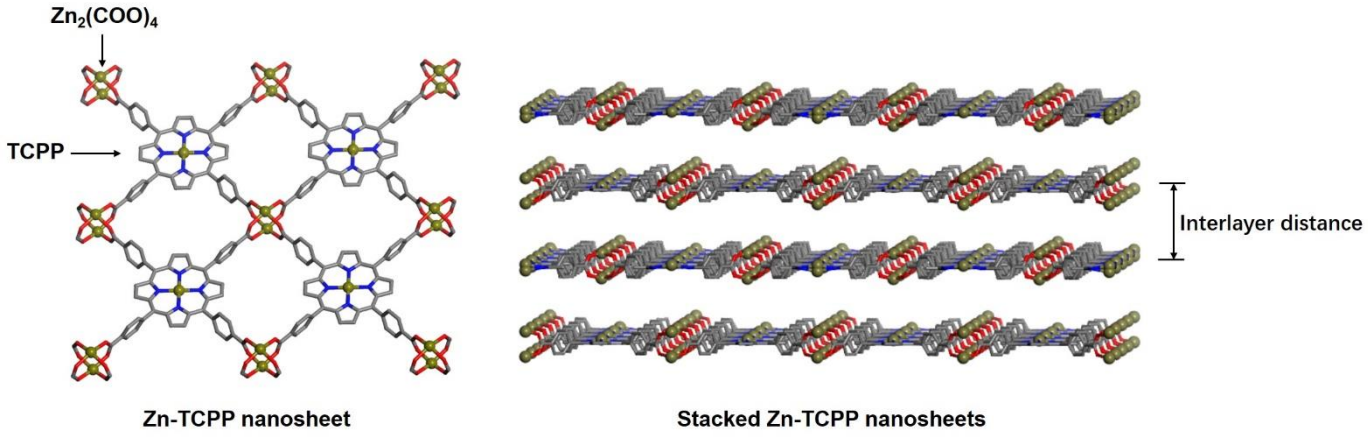

Figure S2. Schematic crystalline structure of Zn-TCPP nanosheets. Zn-TCPP nanosheet is composed of $Zn_2(COO)_4$ paddlewheel metal nodes and TCPP ligand. The interlayer distance between two stacked Zn-TCPP nanosheets is dependent on the conformation of absorbed polymers, and in bulk Zn-TCPP crystal, 0.93 nm [S1]. H atoms have been omitted for clarity.

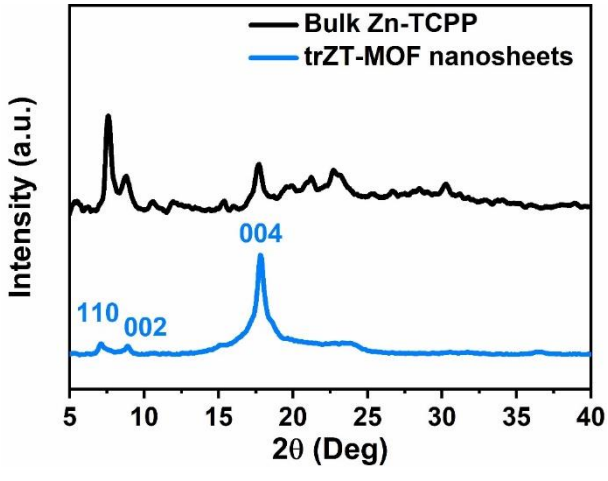

Figure S3. XRD profiles of bulk Zn-TCPP MOF nanoparticles and trZT-MOF nanosheets. trZT-MOF nanosheets show typical (110), (002), and (004) diffractions for Zn-TCPP crystals.[S1]

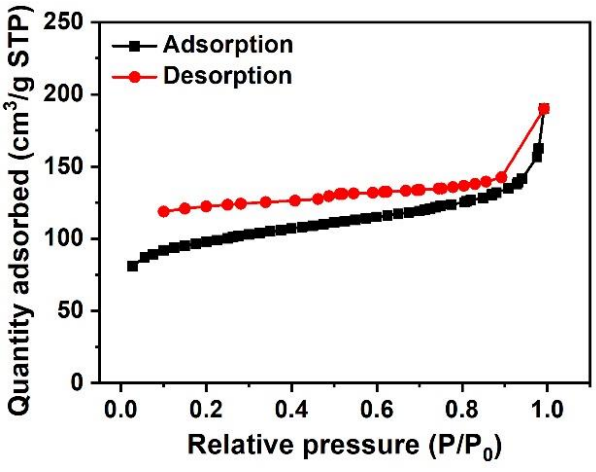

Figure S4. N_2 adsorption-desorption isotherms of trZT-MOF nanosheets.

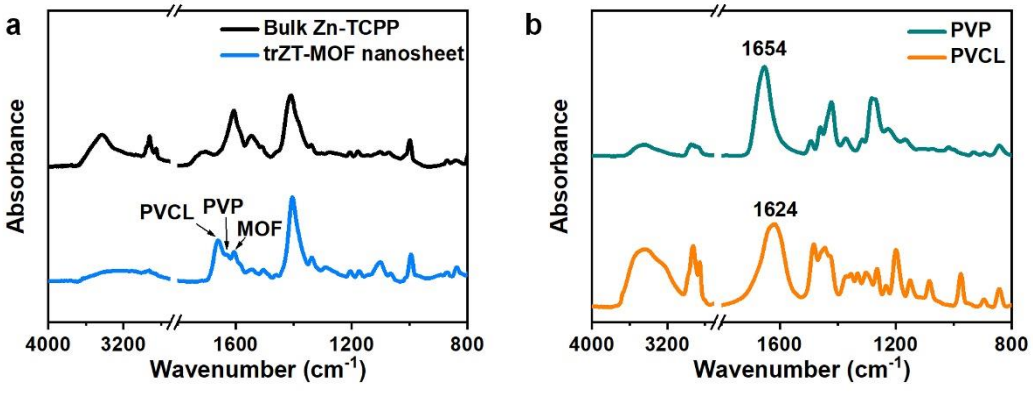

Figure S5. a) FTIR spectra of bulk Zn-TCPP MOF and trZT-MOF nanosheets. b) FTIR spectra of PVP and PVCL.

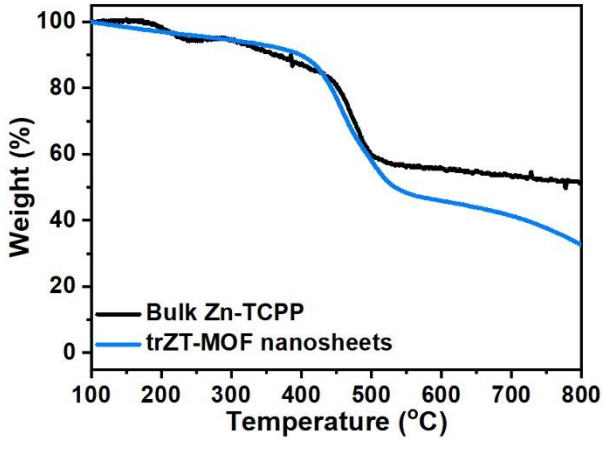

Figure S6 TGA curves of bulk Zn-TCPP MOF and trZT-MOF nanosheets.

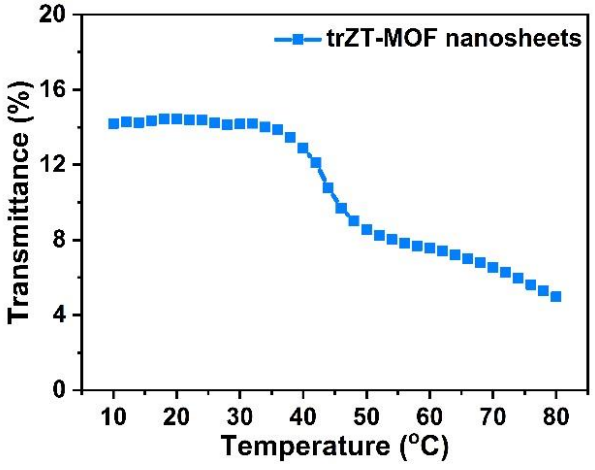

Figure S7. Temperature-dependent turbidity measurement of trZT-MOF nanosheets dispersed in water with the concentration of 10 mg/mL.

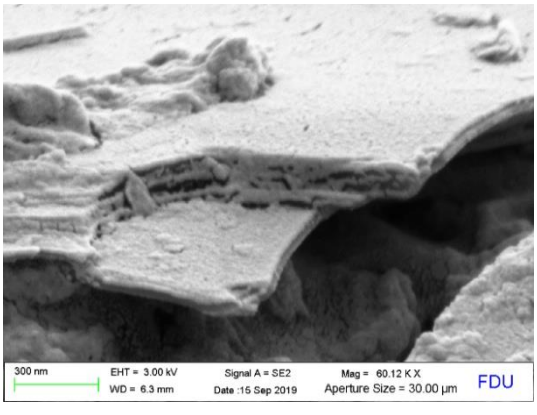

Figure S8. Cross-sectional FE-SEM image of the trZT-MOF nanosheet membrane used for separation tests (thickness ~ 150 nm).

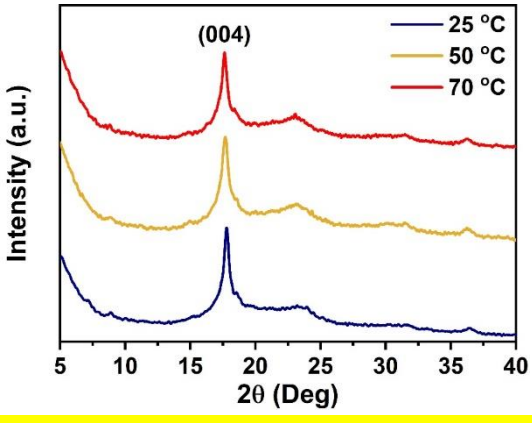

Figure S9. XRD profiles of the trZT-MOF nanosheet membrane after being immersed in water at different temperatures.

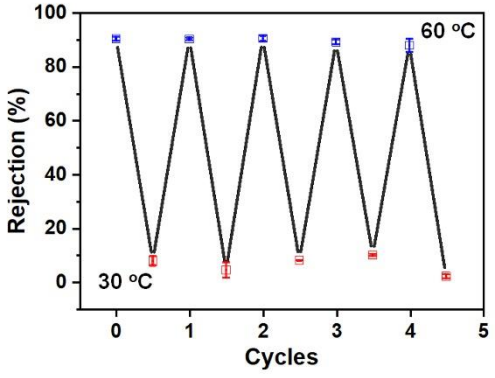

Figure S10. Cyclic rejection test of the trZT-MOF nanosheet membrane upon feeding NR solution at 30 °C and 60 °C.

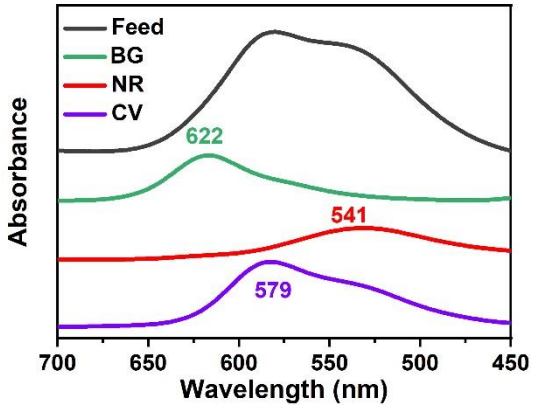

Figure S11. UV/vis spectra of the 10 ppm BG, NR, CV and mixed dye feed solution (NR/CV/BG, 10/10/10 ppm).

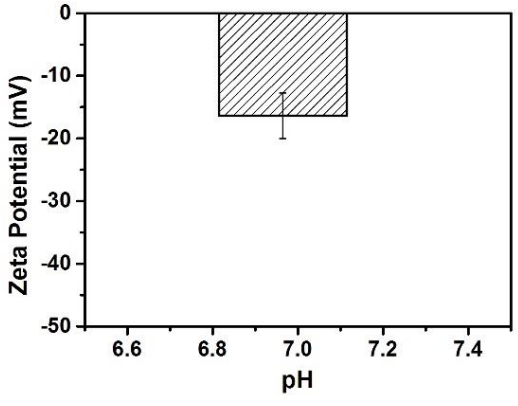

Figure S12. Zeta-potential of trZT-MOF nanosheet membrane shows a low negative charge in neutral water.

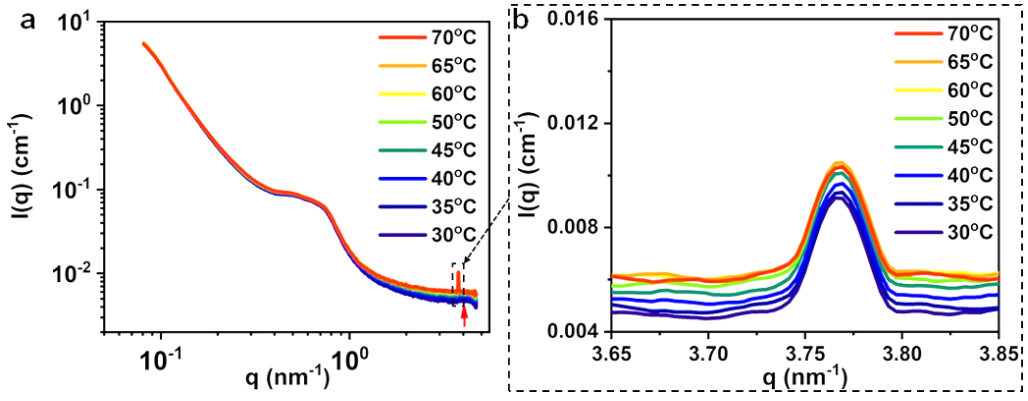

Figure S13. Temperature-dependent overlapped SAXS profiles of trZT-MOF nanosheet membrane from 30 to 70 ℃. (b) is the enlarged view of the rectangular region in (a). In the middle q range (0.4 nm^{-1} < q < 1 nm^{-1}), there is a plateau caused by nylon substrates. In the high q range, there appears a sharp (001) peak of the MOF structure at q = 3.73 nm^{-1}. During heating, almost coincident curves at middle and small q ranges indicate no big changes of the interlayer structure. However, at q > 1 nm^{-1}, the increasing scattering intensities with rising temperature indicate the changes of interfacial properties of trZT-MOF nanosheet membrane. Moreover, there is no changing on the peak position at q ~ 3.73 nm^{-1}, which demonstrates that there are no interlayer distance changes with increasing temperature.

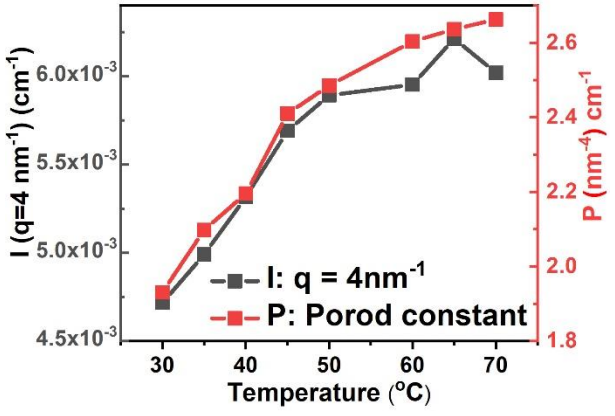

Figure S14. SAXS intensity I (q), (q = 4 nm^{-1}) and SAXS Porod constant (P) plots against temperature of trZT-MOF nanosheet membrane. That the Porod constant (P) increases gradually with the rising temperature indicates the collapse of polymer network on the interface of trZT-MOF nanosheets with increasing specific area.

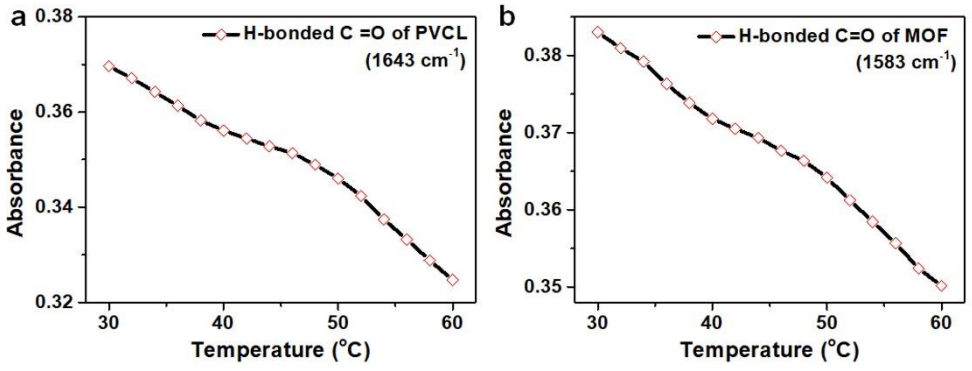

Figure S15. Temperature-dependent absorbance of hydrogen bonded C=O of a) PVCL at 1643 cm^{-1} and b) MOF nanosheets at 1583 cm^{-1} in the trZT-MOF nanosheet membrane.

Table S1. Permeance and separation performance compared with previous reports.

Type	Membrane	Dyes	Operation pressure (bar)	Permeance ($L\ m^{-2}\ h^{-1}\ bar^{-1}$)	Rejection	Ref
MOF nanosheet-based membrane	trZT-MOF nanosheet membrane	Brilliant green	1	854	99.1%	**This work**
		Crystal violet	1	818	99.9%	**This work**
		Neutral Red	1	918	99.0%	**This work**
		Methyl blue	1	764	99.9%	**This work**
GO nanosheet-based membrane	GNM/SWNT	Methyl blue	5	110	96.4%	[S5]
	p-GOM	Rhodamine B-25 °C	1	16.53	68.2%	[S6]
	p-GOM	Rhodamine B-50 °C	1	2.43	100.0%	[S6]
	p-GOM	Coomassie Brilliant Blue-25 °C	1	8.15	98.0%	[S6]
	p-GOM	Coomassie Brilliant Blue-50 °C	1	1.42	100.0%	[S6]
	PEI-GO)/PAA/PVA/GA	Methyl blue	5	0.9	99.3%	[S7]
	brGOM	Methyl blue	3	21.8	99.2%	[S8]
	rGO-TA	Methyl blue	1	2547	76.0%	[S9]
	rGO-GT	Methyl blue	1	189	100%	[S9]
	CDs-GO/MCE	Methyl blue	1	439	94.1%	[S10]
	NSC-GO	rhodamine B	/	279	87.0%	[S11]
Mxene Nanosheet-based membrane	$Ti_3C_2T_x$-NH_2	methyl orange	1-5	1563	73.0%	[S12]
	$Ti_3C_2T_x$-NH_2	methylene blue	1-5	1563	92.0%	[S12]
MOF membrane	ZIF-8/PSS	Methyl blue	5	26.5	98.6%	[S13]
	ZIF-8/PSS	Methyl blue	5	21	98.6%	[S14]
	ZIF-8M	Congo red	2	54.4	99.2%	[S15]
	ZIF-8/PES	Rose bengal	2	37.5	98.5%	[S16]

COF membrane	PEI/ZIF-8/PAN	Congo red	4	37.4	99.2%	[S17]
	COF-LZU1	Methyl blue	5	48.6	99.2%	[S18]
	COF-LZU1	Congo red	5	53.4	98.6%	[S18]
	ГpTGCl@CNFs-5/PAN	Methyl blue	6	75	90.3%	[S19]
	ГpTGCl@CNFs-5/PAN	Congo red	6	79	99.6%	[S19]
	M-TpTD/M-TpBD	Congo red	1	91.62	96.0%	[S20]
	EB-COF:Br	Rhodamine B	0.5	48	91.2%	[S21]

References:

[S1] Zhao, M.; Wang, Y.; Ma, Q.; Huang, Y.; Zhang, X.; Ping, J.; Zhang, Z.; Lu, Q.; Yu, Y.; Xu, H.et al. Ultrathin 2D metal-organic framework nanosheets. *Adv. Mater.* **2015**, *27*, 7372.

[S2] SCHELTEN, J.; SCHMATZ, W. Multiple-scattering treatment for small-angle scattering problems. *J. Appl. Crystallogr.* **1980**, *13*, 385-390.

[S3] Morita, S.; Shinzawa, H.; Noda, I.; Ozaki, Y. Perturbation-correlation moving-window two-dimensional correlation spectroscopy. *Appl. Spectrosc.* **2006**, *60*, 398-406.

[S4] Sun, S.; Wu, P. Spectral insights into microdynamics of thermoresponsive polymers from the perspective of two-dimensional correlation spectroscopy. *Chinese J. Polym. Sci.* **2017**, *35*, 700-712.

[S5] Yang, Y. B.; Yang, X. D.; Liang, L.; Gao, Y. Y.; Cheng, H. Y.; Li, X. M.; Zou, M. C.; Cao, A. Y.; Ma, R. Z.; Yuan, Q.et al. Large-area graphene-nanomesh/carbon-nanotube hybrid membranes for ionic and molecular nanofiltration. *Science* **2019**, *364*, 1057.

[S6] Liu, J. C.; Wang, N.; Yu, L. J.; Karton, A.; Li, W.; Zhang, W. X.; Guo, F. Y.; Hou, L. L.; Cheng, Q. F.; Jiang, L.et al. Bioinspired graphene membrane with temperature tunable channels for water gating and molecular separation. *Nat. Commun.* **2017**, *8*, 2011.

[S7] Wang, N. X.; Ji, S. L.; Zhang, G. J.; Li, J.; Wang, L. Self-assembly of graphene oxide and polyelectrolyte complex nanohybrid membranes for nanofiltration and pervaporation. *Chem. Eng. J.* **2012**, *213*, 318-329.

[S8] Han, Y.; Xu, Z.; Gao, C. Ultrathin graphene nanofiltration membrane for water purification. *Adv. Funct. Mater.* **2013**, *23*, 3693-3700.

[S9] Thebo, K. H.; Qian, X.; Zhang, Q.; Chen, L.; Cheng, H.; Ren, W. Highly stable graphene-oxide-based membranes with superior permeability. *Nat. Commun.* **2018**, *9*, 1486.

[S10] Wang, W.; Eftekhari, E.; Zhu, G.; Zhang, X.; Yan, Z.; Li, Q. Graphene oxide membranes with tunable permeability due to embedded carbon dots. *Chem. Commun.* **2014**, *50*, 13089-13092.

[S11] Huang, H.; Song, Z.; Wei, N.; Shi, L.; Mao, Y.; Ying, Y.; Sun, L.; Xu, Z.; Peng, X. Ultrafast viscous water flow through nanostrand-channelled graphene oxide membranes. *Nat. Commun.* **2013**, *4*, 2979.

[S12] Wu, X.; Cui, X.; Wu, W.; Wang, J.; Li, Y.; Jiang, Z. Elucidating ultrafast molecular permeation through well-defined 2d nanochannels of lamellar membranes. *Angew. Chem., Int. Ed.* **2019**, *58*, 18524-18529.

[S13] Zhang, R.; Ji, S. L.; Wang, N. X.; Wang, L.; Zhang, G. J.; Li, J. R. Coordination-driven in situ self-assembly strategy for the preparation of metal-organic framework hybrid membranes. *Angew. Chem., Int. Ed.* **2014**, *53*, 9775-9779.

[S14] Wang, N. X.; Liu, T. J.; Shen, H. P.; Ji, S. L.; Li, J. R.; Zhang, R. Ceramic tubular MOF hybrid membrane fabricated through in situ layer-by-layer self-assembly for nanofiltration. *AICHE J.* **2016**, *62*, 538-546.

[S15] Li, Q.; Li, J. S.; Fang, X. F.; Liao, Z. P.; Wang, D. P.; Sun, X. Y.; Shen, J. Y.; Han, W. Q.; Wang, L. J. Interfacial growth of metal-organic framework membranes on porous polymers via phase transformation. *Chem. Commun.* **2018**, *54*, 3590-3593.

[S16] Li, Y.; Wee, L. H.; Martens, J. A.; Vankelecom, I. Interfacial synthesis of ZIF-8 membranes with improved nanofiltration performance. *J. Membr. Sci.* **2017**, *523*, 561-566.

[S17] Yang, L. B.; Wang, Z.; Zhang, J. L. Zeolite imidazolate framework hybrid nanofiltration (NF) membranes with enhanced permselectivity for dye removal. *J. Membr. Sci.* **2017**, *532*, 76-86.

[S18] Fan, H. W.; Gu, J. H.; Meng, H.; Knebel, A.; Caro, J. High-flux membranes based on the covalent organic framework cof-lzu1 for selective dye separation by nanofiltration. *Angew. Chem., Int. Ed.* **2018**, *57*, 4083-4087.

[S19] Yang, H.; Yang, L. X.; Wang, H. J.; Xu, Z.; Zhao, Y. M.; Luo, Y.; Nasir, N.; Song, Y. M.; Wu, H.; Pan, F. S.et al. Covalent organic framework membranes through a mixed-dimensional assembly for molecular separations. *Nat. Commun.* **2019**, *10*, 2101.

[S20] Kandambeth, S.; Biswal, B. P.; Chaudhari, H. D.; Rout, K. C.; Kunjattu, H. S.; Mitra, S.; Karak, S.; Das, A.; Mukherjee, R.; Kharul, U. K.et al. Selective molecular sieving in self-standing porous covalent-organic-framework membranes. *Adv. Mater.* **2017**, *29*, 1603945.

[S21] Zhang, W. X.; Zhang, L. M.; Zhao, H. F.; Li, B.; Ma, H. P. A two-dimensional cationic covalent organic framework membrane for selective molecular sieving. *J. Mater. Chem. A* **2018**, *6*, 13331-13339.